AIP | Review of Scientific Instruments

Spatio-temporal measurements of Trichel corona discharge using capacitive probe diagnostic

Deepak K. Gupta, H. Ramachandran, and P. I. John

Citation: Review of Scientific Instruments **71**, 406 (2000); doi: 10.1063/1.1150215
View online: http://dx.doi.org/10.1063/1.1150215
View Table of Contents: http://scitation.aip.org/content/aip/journal/rsi/71/2?ver=pdfcov
Published by the AIP Publishing

Spatio-temporal measurements of Trichel corona discharge using capacitive probe diagnostic

Deepak K. Gupta,[a] H. Ramachandran, and P. I. John
Institute for Plasma Research, Bhat, Gandhinagar, India

(Received 18 June 1999; accepted for publication 8 November 1999)

A nonintrusive capacitive probe diagnostic is developed to estimate the spatio-temporal charge density variation of corona discharge. Tikhonov regularization is used to calculate the charge density from measured potential. A good time resolution and restricted space resolution in charge density is achieved. The axial electric field due to space charge is also estimated by considering the discharge to be of finite radius and with uniformly distributed charge density along the radial direction. Space charge wave front movement, as predicted by existing theories, is noticed. Constraints of present technique and scope for further improvements are discussed. © *2000 American Institute of Physics.* [S0034-6748(00)04702-X]

I. INTRODUCTION

The capacitive probe diagnostic has been widely used in the gas discharge and electron beam physics for a long time. As a beam diagnostic it has been used to get the information about beam profile, beam position, charge, length,[1–3] drift velocity,[4] etc. It has also been used to diagnose radio-frequency (rf),[5,6] Q-machine,[7] and even Tokamak[8] plasmas. The use of capacitive probe diagnostics for spatio-temporal studies is also not new. Choi and Favre [9] in hollow cathode discharge and Anikin *et al.*[10] in high voltage breakdown have used them for similar studies.

Due to small discharge size and nonuniform discharge profile, electrical probe diagnostics have not been widely used in electrical corona discharge. A brief review of probe diagnostics in corona discharge may be found in Ref. 11. Probe diagnostics in these discharges can be divided into the two general types; Langmuir probes where the main signal is due to conduction current, and capacitive probes where the displacement current contributes to the signal. Other than estimating the electric field, Langmuir probes have been used to estimate the particle current densities in the drift region of corona.[12,13] However these measurements are not free from distortion due to probe itself. Capacitive probes have the advantage of being nonintrusive due to their very high input impedance. However they have only been used for the estimation of temporal electric field profile on electrodes in direct-current (dc) as well as alternating-current (ac) corona.[11]

Here we present our attempts to use a nonintrusive, capacitive probe diagnostic for the spatio-temporal study of a negative corona discharge. As our probes are situated outside the discharge volume and path, the distortion in the measurements is negligible. This diagnostic is able to provide an estimation of charge density and axial space charge electric field. The velocity of the weak space charge wave front, moving towards the plane electrode is also estimated. Other than the capacitive probe diagnostic, these types of measurements are possible using spectroscopy or optical diagnostics where instrument cost and system complexity is large. In the present work, two circular probes are used, that are movable along the axis of the discharge. It is shown that the space charge density is related to the measured potential through an integral equation. The charge density is obtained by solving the integral equation numerically and the axial electric field is estimated using the method of disks.[14]

The description of the discharge assembly and probe construction is discussed in Sec. II. The basic principle and method applied to the probe configuration is presented in Sec. III. Calibration of probes in Sec. IV is followed by results and discussions in Sec. V.

II. DISCHARGE ASSEMBLY AND PROBE CONSTRUCTION

The schematic of experimental setup, along with capacitive probes is shown in Fig. 1. A Trichel corona discharge[15] is created in a needle-plane geometry by keeping the needle electrode at negative potential with respect to a plane electrode. A positive high voltage is applied to the plane electrode through a current limiting resistance. The needle electrode is grounded through a 50 Ω resistance, and signal was carried to the oscilloscope using a matched coaxial cable of length about a meter.

A capacitive probe pair is made on a perspex cylinder (wall thickness 3 mm, inner diameter 51 mm) concentric to both the electrodes and movable along the discharge axis. Two grooves (depth about a mm) are made along the circumference of the outer curved surface of the cylinder, at a separation of 20 mm from each other. The capacitive probes are constructed by winding a single turn closed loop copper wire (diameter 0.5 mm) in each groove. Both the winding in the grooves are covered with insulation before covering the whole outer curved surface of perspex cylinder with grounded copper foil. The probes are connected separately to this grounded foil through 50 Ω measuring resistances, and signal was carried to the oscilloscope using a matched co-

[a]Electronic mail: deepak@plasma.ernet.in

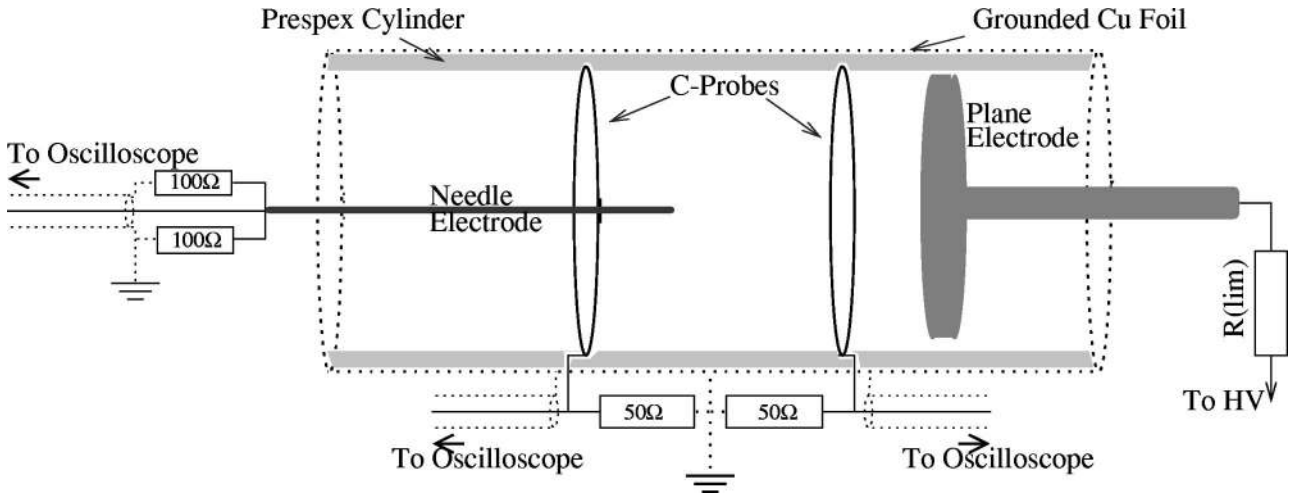

FIG. 1. Schematic of capacitive probes and discharge electrode assembly in experiment.

axial cable of length about a meter. Probes were designed in such a way that its capacitance with ground is more than its capacitance with electrodes, but its RC time constant is much less than any characteristics time of interest.[9] Signals were acquired using an 500 MHz digital oscilloscope at the real-time sampling rate of one gigasample per seconds (1 GS/s). The probe assembly is movable with a resolution of 1 mm along the discharge axis for spatial measurements.

The electrodes and the probe assembly are kept inside a perspex chamber, filled with dry air after evacuating it to 10^{-3} Torr. The operating pressure is measured using mercury manometer.

III. BASIC PRINCIPLE AND METHOD

The circuit current through the measuring resistance is given by

$$i_p(t)=A_p\frac{\partial\sigma(t)}{\partial t}=A_p\epsilon_o\frac{\partial E_n(t)}{\partial t}$$

$$=-A_p\epsilon_o\frac{\partial}{\partial t}\nabla_n(\phi_l+\phi_s), \tag{1}$$

where A_p is the surface area of the capacitive probe, $\sigma(t)$ is the surface charge induced per unit area on the probe surface, ϵ_o is the free space permittivity, $E_n(t)$ is the electric field normal to the probe surface, ϕ_l and ϕ_s are the Laplacian and space charge potentials, respectively. Noting that ϕ_l is time independent, we get

$$i_p(t)=-\epsilon_o A_p\frac{\partial}{\partial t}\nabla_n(\phi_s). \tag{2}$$

Corona discharge is considered as an axially symmetric cylinder with uniform radial distribution and variable axial distribution of charge. As the probe is also in the form of an axially symmetric metallic circular loop, the normal surface vector $\hat{n}=-\hat{r}$ (refer to Fig. 2), hence Eq. (2) reduces to

$$\frac{\partial\phi_s}{\partial r}=\frac{1}{\epsilon_o A_p}\int_0^t i_p(t)dt. \tag{3}$$

For a probe situated at (r,z) the space charge potential can be written as

$$\phi_s(r,z,t)=\int_0^L G(r,z,z')\rho(z',t)dz' \tag{4}$$

using line charge density ρ. The one-dimensional Green function G is the potential at (r,z) inside a grounded cylinder defined by the boundaries $z=0$, $z=L$, $r=a$, due to a point charge located at z' on the axis $(r'=0)$,[16] i.e.,

$$G(r,z,z')=\frac{1}{\pi\epsilon_o L}\sum_{n=1}^{\infty}R_n(r)\sin(k_n z)\sin(k_n z'), \tag{5}$$

where, $k_n=n\pi/L$, and R_n, the radial component of the Green function is given by

$$R_n(r)=\left[K_0(k_n r)-\frac{K_0(k_n a)I_0(k_n r)}{I_0(k_n a)}\right], \tag{6}$$

where, K_0 and I_0 are the modified Bessel functions of order zero. Substituting Eq. (4) in Eq. (3), yields to a Fredholm integral equation of the first kind, i.e.,

$$f(z)=\int_0^L \mathcal{K}(z,z')\,\rho(z')dz', \tag{7}$$

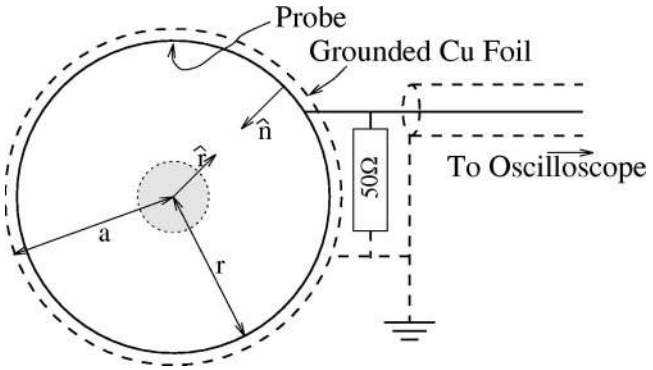

FIG. 2. Schematic axial view of capacitive probe. The plasma is indicated by the shaded region in the center. The probe is located at a distance r from the center, near the grounded wall (radius a). Probe is grounded through 50 Ω measuring resistance.

where

$$f(z)=\int_0^t i_p(t)dt, \tag{8}$$

the time integral of the current of the probe at z, and

$$\mathcal{K}(z,z')=-\frac{A_p}{L^2}\int_0^L\sum_{n=1}^{\infty} n\left[K_1(k_n r)+\frac{K_0(k_n a)I_1(k_n r)}{I_0(k_n a)}\right]\times\sin(k_n z)\sin(k_n z')\,dz' \tag{9}$$

are known for $0<z<L$. In the above equation, K_1 and I_1 are the modified Bessel functions of order one.

To get the linear charge density ρ one has to solve the integral Eq. (7), where $f(z)$ is known from experiment at some finite points and kernel $\mathcal{K}(z,z')$ is defined analytically in the region of interest. It can be understood from Eq. (7) that probe signal (or, more accurately, time integral of the probe signal) is due to combination (or integration) of all the charge density in the gap. Hence any sharp changes or small spatial fluctuations in the charge density will be smoothed, and their information will be lost in measured signal. Solving an integral equation means to retrieve the information from this averaged signal. The situation becomes further complicated due to unavoidable noise always present in the measurements. This mostly misleads the solution of integral equation to the unacceptable limits. Special numerical techniques have been developed for solving these ''ill conditioned'' problems.[17] Tikhonov regularization is one of the most popular techniques for these problems.[17] In this method, minimization of a linear set of algebraic equation arising due to discretization of Fredholm equation of the first kind, along with a smoothing function with a weightage parameter, is done. The weightage parameter, also known as regularization parameter, is estimated using the *L*-curve method, suggested by Hansen,[17] which gives an optimum balance between maximum smoothing and nonsmoothing solution.

For calculating the axial space charge electric field, one should actually solve the Poisson equation in three dimension. We have used the disk method proposed by Davies *et al.*[14] for evaluating the axial electric field. In this method, discharge is considered as a cylinder of finite radius and the charges are uniformly distributed over the radial cross-section and varying only in the axial direction. This method has been widely used for calculating the space charge electric field in gas discharge modeling including corona discharge.[14,18,19] The method incorporates the effect of boundary conditions by considering the image charges due to discharge in conducting electrodes. Using the disk method, the axial space charge electric field can be represented as

$$E_s(z)=\frac{1}{2\epsilon_o}\left[\int_{-z}^{0}\rho(z+z')\left(-1-\frac{z'}{\sqrt{z'^2+r_d^2}}\right)dz'+\int_0^{L-z}\rho(z+z')\left(1-\frac{z'}{\sqrt{z'^2+r_d^2}}\right)dz'\right], \tag{10}$$

where r_d is the radius of the discharge.

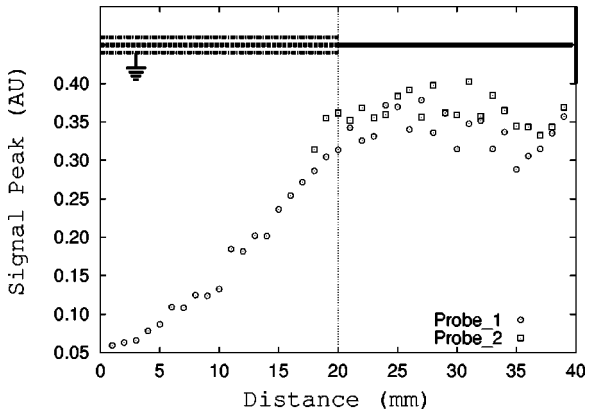

FIG. 3. (Top of figure) Calibration assembly used to calibrate the capacitive probes. A grounded braid covers a wire biased to 15 V, from $z=0$ to 20 mm. The wire is exposed from $z=20$ to 40 mm. (Bottom of the figure) Probe response to biased wire in arbitrary units. Circles represent probe 1 while boxes represent probe 2.

IV. PROBE CALIBRATION

For the probe calibration, the needle electrode and discharge gap (total length 40 mm) is replaced by a half striped coaxial cable whose outer metallic braid shield along with inner and outer insulations of half length (20 mm) is removed to expose the inner conductor. The other half (20 mm) of this coaxial cable is kept as it is with outer metallic braid shield grounded. The schematic of this is shown in the upper part of Fig. 3. This half striped coaxial cable was kept coaxial to the circular capacitive probes and positioned along the axial direction in such a way that the exposed unbraided inner conductor occupied the space taken by the discharge gap (position 20–40 mm) in actual discharge assembly. And the covered braid cable, with grounded braid, took the position of grounded needle electrode (position 0–20 mm) in actual discharge assembly. The probe signals were measured at various axial locations when a rectangular voltage pulse of width about 500 ns and amplitude 15 V was applied to the exposed (unbraided) cable having a diameter of 1.6 mm. Figure 3 shows the comparative signal strength from both the probes at different locations. The approximately equal response of both the probes, in the region 20–40 mm shows that the two probes can be regarded as identical. During probe calibration signals with rise times of 10 ns were correctly measured using capacitive probe. This time is about two to three times faster as compared to the rise time of the corona discharge pulse at 50 Torr, studied in the present work

Figure 4 shows spatial variation of the linear charge density at different times using the regularization technique applied to probe measurements of the voltage pulse and Fig. 5 shows its temporal variation at different locations. A uniform grid with a resolution of 1 mm in the complete region of 40 mm, was considered to estimate this charge density profile from 63 spatial measurements. The choice of the regularization grid resolution was based upon the measurement resolution and the requirement of Tikhonov method that the number of measurement points should be more than or at least equal to the number of unknowns (i.e., charge density at grid point).

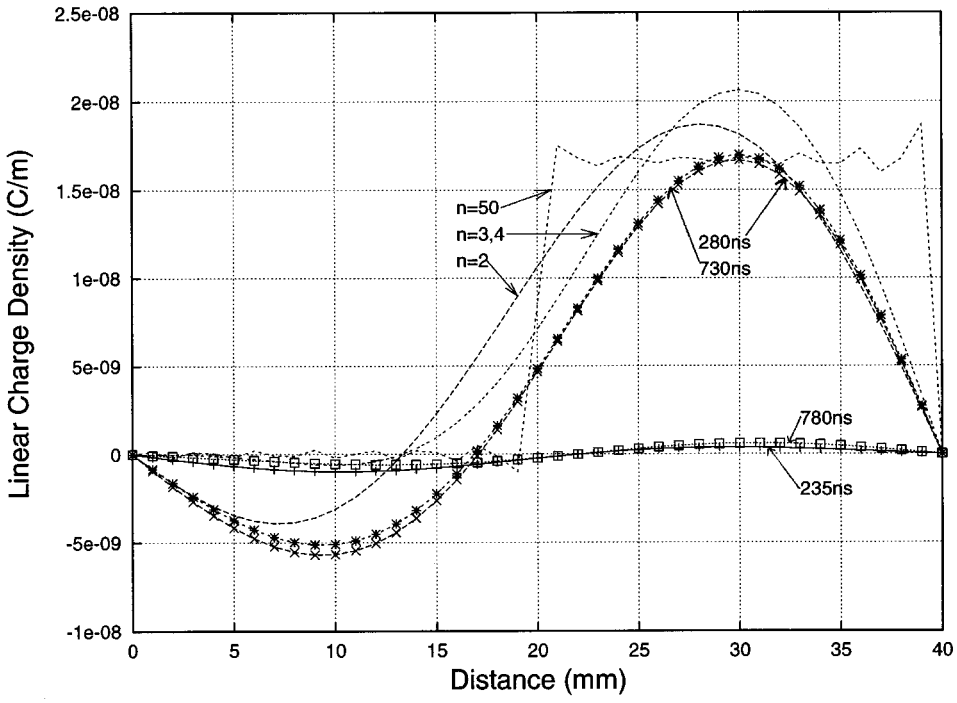

FIG. 4. Comparison of analytically calculated charge density with the experimentally measured profile [calculated by numerically solving integral Eq. (7)] of calibration charge. (The charge density is varied as shown in Fig. 5.) Lines without symbols show the analytical approximation of the known charge profile at $t=500$ ns summed up to the n mode indicated with each line. Lines with symbols show the experimental estimation of charge density for the time indicated on each curve.

As charge density $\rho(z)$ vanishes at the electrodes boundaries it is considered as the sum of sine series with appropriate coefficients, a_l,

$$\rho(z)=\sum_{l=1}^{\infty} a_l \sin(k_l z). \tag{11}$$

Substituting this in the integral Eq. (4) and applying the orthogonality conditions along with the appropriate boundary conditions for exposed unbraided cylindrical inner conductor

$$\phi_s(r,z)=0; \quad 0<z<L/2,$$
$$\phi_s(r=r_0,z)=V_0; \quad L/2<z<L, \tag{12}$$

where V_0 is the applied potential and r_0 is the radius of exposed unbraided inner conductor, lead to the coefficients

$$a_l=\frac{2\pi\epsilon_0 V_0}{k_l R_l(r)}[\cos(l\pi/2)-\cos(l\pi)], \tag{13}$$

where $R_l(r)$ is given by Eq. (6).

According to the configuration used for the probe calibration, the charge density is expected to be zero from location 0 to 20 mm and have a constant positive value from 20 to 40 mm. This also implies that there will be a sharp jump in the charge density at or around 20 mm. Analytically calculated approximation of the charge density, $\rho_n(z)$

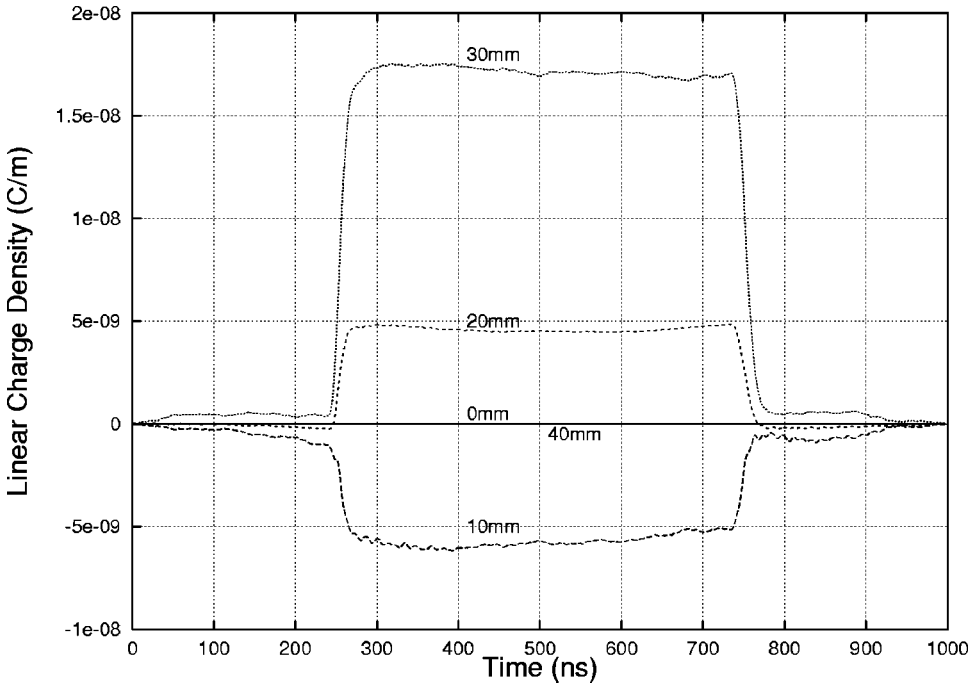

FIG. 5. Time variation of charge density on the calibration wire when a step voltage of width 500 ns is applied on it, estimated by inverting experimental measurements at different locations.

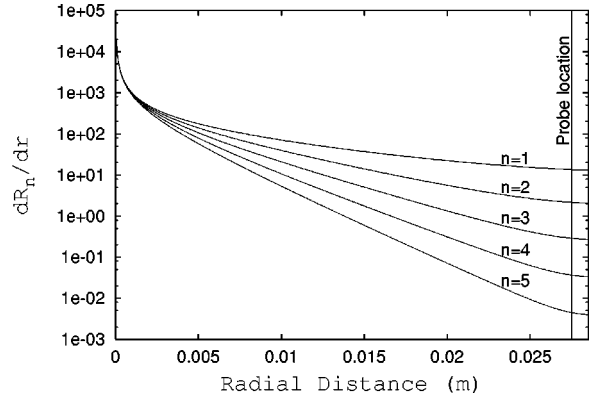

FIG. 6. Radial decay of $\partial R_n/\partial r$ for different modes. $\partial R_n/\partial r$ is directly related to the signal strength. Vertical line on the right side of the graph indicates the location of the probe.

$=\Sigma_{l=1}^{n} a_l \sin(k_l z)$ for mode numbers, $n=1$, 2, 3, 4, and 50 are shown in Fig. 4. This shows that the estimated solution using regularization matches fairly well with the analytical solutions for $n=2$ to 4 modes. Small variation from these modes in the central region is due to regularization's smoothing effect of the sharp step at $z=20$ mm. Although Tikhonov regularization technique is capable of giving the solution quite near to the ''actual'' solution of integral equation, it smooths the sharp changes and small fluctuations. Also in the attempt of finding a smooth continuous function around the large amplitude sharp changes, solution may show the overshoot or nonphysical solution around the sharp variation point. However, it is clear from Fig. 4 that capacitive probe diagnostic can yield a good estimate of charge density. Figure 5 shows the fast rise and fall in charge density with good flat top according to the voltage present on the test conductor. This indicates the ability of present technique to reproduce an excellent temporal variation of charge density profile.

Equation (2) shows that the probe current (or signal strength) directly depends upon $\partial R_n/\partial r$, where R_n represents the radial component of the Green's function [Eq. (6)]. In Fig. 6, the individual terms corresponding to the first few

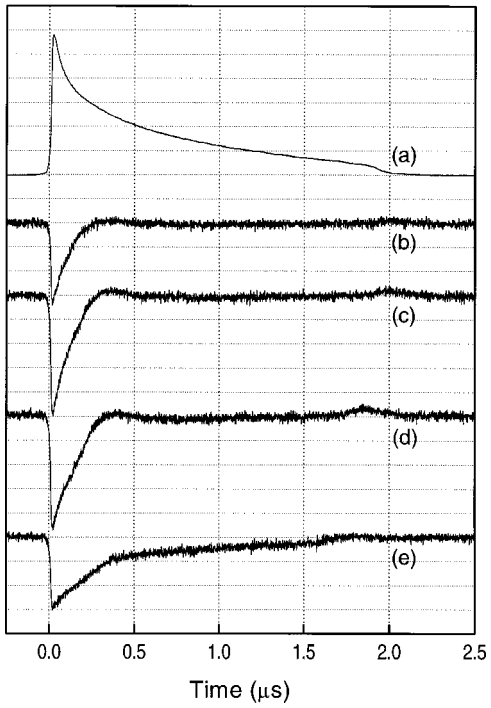

FIG. 7. (a) A typical discharge current pulse; 0.4 mA/div and *C*-probe signal at (b) 12, (c) 20 (nearest to needle tip), (d) 28, and (e) 36 mm (near to plane); (b)–(e) 0.02 mA/div. Data are acquired up to 3.6 μs, however no appreciable signal is observed after 2.1 μs.

modes have been plotted against radial distance. It can be seen from this graph that even for the $n=1$ mode, the quantity $\partial R_n/\partial r$, and hence the signal strength, is three orders less at the probe location compared to the center $(r=0)$ where the modes are generated (or the discharge is located). Moreover, the signal from each successive mode at the same probe location reduces by an order of magnitude. As can be observed from the probe signals shown in Fig. 7, the typical signal-to-noise ratios (S/N) are around 10 to 30. Hence any mode that has an amplitude comparable to or less than the (S/N) times the amplitude of first mode, will be buried in the noise itself. This is probably the reason why the regulariza-

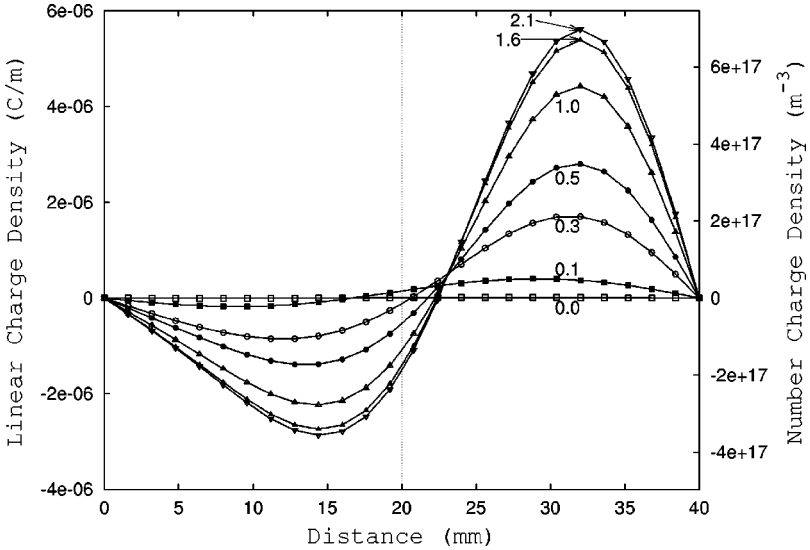

FIG. 8. Spatial variation of charge density in a corona discharge. The needle electrode spanned from 0 to 20 mm, with sharp edge at 20 mm. Plane is located at 40 mm. Time is indicated on each curve in microseconds.

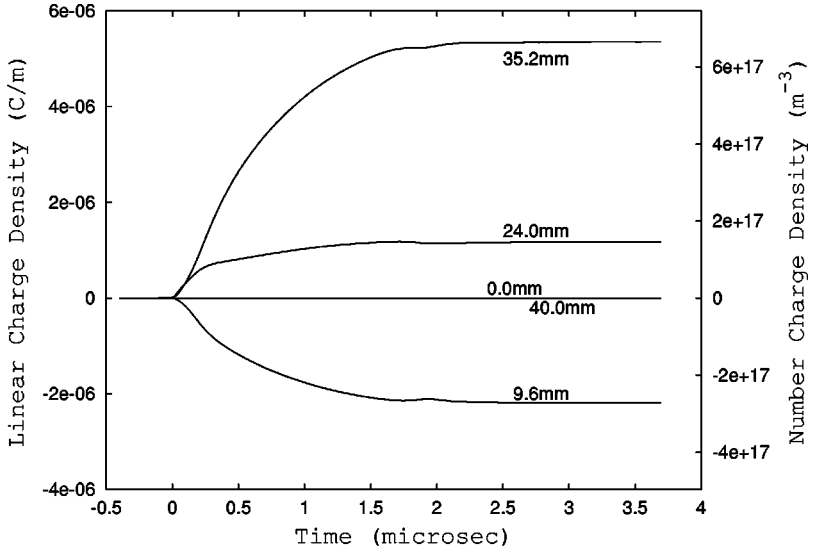

FIG. 9. Temporal variation of charge density in a corona discharge. The *y* axis on the right hand side shows the number density considering the discharge to have uniform charge density across the radius of 1 mm. Gap location according to Fig. 8 is indicated on each line.

tion solution shows best agreements with low *n* approximations of the charge density.

V. RESULTS AND DISCUSSION

Trichel corona pulses were produced at a pressure of 50 Torr, with a hemispherical tip needle of diameter 2 mm, kept at distance of 20 mm from the plane electrode. In the experimental assembly, the needle electrode spanned from 0 to 20 mm. The discharge occurred in the gap between the needle tip (at 20 mm) and the plane electrode (at 40 mm). Measurements were made along the total axial length of 40 mm with a resolution of 1 mm. The charge density profile was estimated in the complete region using uniform grid resolution of 1.6 mm.

Typical corona current pulse and capacitive probe signals are shown in Fig. 7. Other than the change in pulse shape, the probe signal amplitude decreases as probe is moved away on either side of the hemispherical tip of needle electrode, along the axial direction. In addition, the nature of the probe signal also varies with probe location.

Figure 8 shows the spatial distribution of charge density at various times. The number density (i.e., charge particles per unit volume) is indicated on the right hand *y* axis of the figure. The number density was obtained by considering the discharge to have uniform radial charge density of a radius of 1 mm. This number density is used to estimate the axial electric field due to space charge [using Eq. (10)].

The temporal variation of charge density at different locations is plotted in Fig. 9. The charge density is seen to rise with the initiation of the corona discharge and increases with time to attain a maximum value in about 2.1 μs, after which it remains approximately steady.

The charge density curves in the Fig. 8 indicate that the maximum charge density, and hence the discharge, is present in the discharge gap region of 20–40 mm. According to the previous simulation and experimental works,[15,19] one expected to get the plasma (with zero electric field in it) in front of the needle along with the steep change in charge density towards the needle tip (i.e., 20 mm). Negative charge density, instead of zero charge density, in the region of grounded needle electrode (i.e., 0–20 mm) is observed.

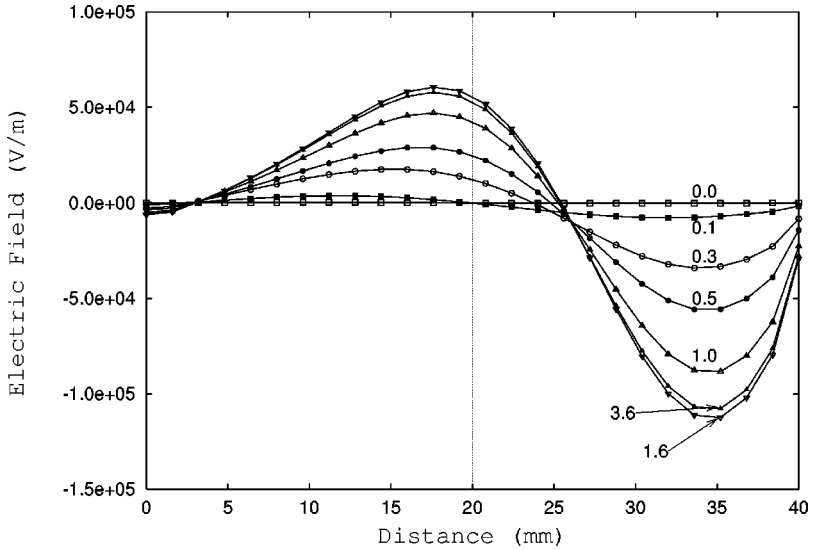

FIG. 10. Spatial variation of axial electric field in a corona discharge. The needle electrode spanned from 0 to 20 mm, with sharp edge at 20 mm. Plane is located at 40 mm. Time is indicated on each curve in microseconds.

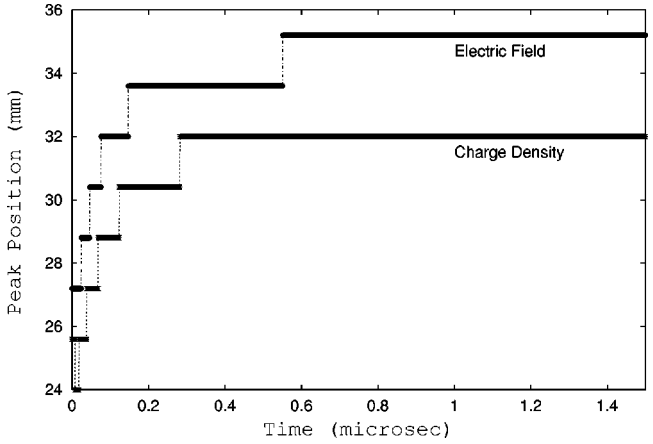

FIG. 11. Location of peaks of charge density and electric field vs time. Electric field peak is always ahead in space than charge density peak. The movement is fast initially and then slows down.

Deviations from expected results are probably due to two reasons, already discussed in probe calibration section (Sec. IV). First due to inability of the present method to reproduce the higher modes, and second due to the smoothing effect of regularization of the sharp gradient around the needle tip (i.e., $x=20$ mm) location. Other than these, the low spatial resolution (1.6 mm) used in the regularization, to construct the density profile, also restricted the spatial resolution of the obtained results. This spatial resolution limit is due to the spatial measurement resolution of 1 mm. However it is clear from Sec. IV that even with these restrictions the present method is able to provide fairly accurate estimates of the charge density.

Assuming a uniform discharge radius of 1 mm and the data from Fig. 8 the maximum number density is obtain to be of the order of $10^{17}\,m^{-3}$ which is very similar to the charge density shown by the simulation results by Morrow[19] at 50 Torr with the discharge radius of 4 mm.

Figure 10 presents the axial electric field [from Eq. (10)] due to space charge as function of position. As expected from the charge density profile (Fig. 8), a strong electric field is present in the discharge gap region (i.e., 20–40 mm). Figure 11 tracks the location of the space charge density and electric field peaks during the growth part of the discharge. Initially, the peaks move quickly, and gradually slow down and finally stop. It is to be noticed that the peak of electric field is always ahead and moves faster than the charge density peak. Existing theories of corona discharge predict space charge wave front that moves towards the plane electrode and weakens in time.[19] The current observations confirm these theoretical predictions. The average velocity of the space charge wave front estimated from Fig. 11 is approximately 10^4 m/s, an order of magnitude less than the previous simulation results.[19,20]

The time variation of the total charge, estimated from the capacitive probe and from discharge current, is shown in Fig. 12. The total charge estimated from the capacitive probe is slightly lower but of the same order as that from the discharge current. This discrepancy is probably due to the missing higher order spatial modes.

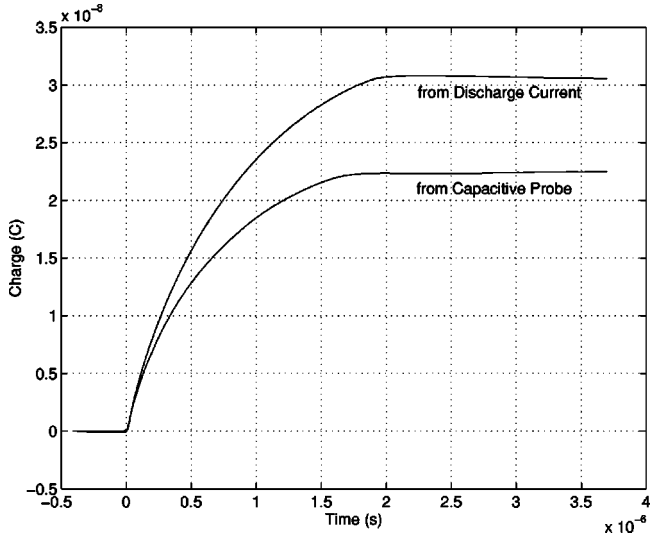

FIG. 12. Comparison of total charge estimated from discharge current and capacitive probe.

The spatial resolution measurements can be improved by designing a probe having a better resolution in axial movement. As the regularization method is based on the least square minimization technique itself, a large data set can yield better results. Also, because of the highly nonuniform discharge profile, use of a regularization technique based on a nonuniform grid rather than a uniform grid can help to improve the quality of the spatial measurements.

ACKNOWLEDGMENTS

D. K. G. and P. I. J. would like to thank Dr. S. V. Kulkarni for helping in understanding the corona discharge and in setting up the corona experiment.

[1] J. Gilpatrick and C. DD, IEEE Trans. Nucl. Sci. **NS-32**, 1962 (1985).
[2] J. Gilpatrick and C. Watson, IEEE Trans. Nucl. Sci. **NS-32**, 1965 (1985).
[3] A. Van der Meer, R. Bakker, C. Van der Geer, and P. Van Amersfoort, Rev. Sci. Instrum. **62**, 2904 (1991).
[4] P. Avivi, C. Cohen, and L. Friedland, Appl. Phys. Lett. **42**, 948 (1983).
[5] S. Sevas and K. Donohoe, Rev. Sci. Instrum. **60**, 3391 (1989).
[6] J. Wilson, J. Caughman II, P. L. Nguyen, and D. Ruzic, J. Vac. Sci. Technol. A **7**, 972 (1989).
[7] N. Benjamin, Rev. Sci. Instrum. **53**, 1541 (1982).
[8] E. Wang *et al.*, Rev. Sci. Instrum. **62**, 1494 (1991).
[9] P. Choi and M. Favre, Rev. Sci. Instrum. **65**, 2281 (1994).
[10] N. Anikin, S. Pancheshnyi, S. Starikovskaia, and A. Starrikovskii, J. Phys. D: Appl. Phys. **31**, 826 (1998).
[11] R. Waters, in *Electrical Breakdown and Discharges in Gases; Part B*, edited by E. Kunhardt and L. Luessen (Plenum, New York, 1983), p. 203.
[12] S. Masuda and Y. Nonogaki, J. Electrost. **10**, 73 (1981).
[13] J. Cross and N. Barton, J. Electrost. **15**, 15 (1984).
[14] A. Davies, C. Evans, and F. Llewellyn-Jones, Proc. R. Soc. London, Ser. A **281**, 164 (1964).
[15] G. Trichel, Phys. Rev. **54**, 1078 (1938).
[16] J. Jackson, in *Classical Electrodynamics*, 2nd ed. (Wiley, New York, 1975), Chap. 3, p. 134.
[17] P. Hansen, Inverse Probl. **8**, 894 (1992).
[18] A. Davies, C. Evans, and P. Woodison, Proc. IEE **122**, 765 (1975).
[19] R. Morrow, Phys. Rev. A **32**, 1799 (1985).
[20] E. Kunhardt and Y. Tzeng, Phys. Rev. A **38**, 1410 (1988).